

Tuning element distribution, structure and properties by composition in high-entropy alloys

Qingqing Ding^{1,9}, Yin Zhang^{2,9}, Xiao Chen^{3,9}, Xiaoqian Fu¹, Dengke Chen², Sijing Chen¹, Lin Gu⁴, Fei Wei³, Hongbin Bei¹, Yanfei Gao^{5,6}, Minru Wen², Jixue Li¹, Ze Zhang¹, Ting Zhu^{2*}, Robert O. Ritchie^{7,8*} & Qian Yu^{1*}

High-entropy alloys are a class of materials that contain five or more elements in near-equiatomic proportions^{1,2}. Their unconventional compositions and chemical structures hold promise for achieving unprecedented combinations of mechanical properties^{3–8}. Rational design of such alloys hinges on an understanding of the composition–structure–property relationships in a near-infinite compositional space^{9,10}. Here we use atomic-resolution chemical mapping to reveal the element distribution of the widely studied face-centred cubic CrMnFeCoNi Cantor alloy² and of a new face-centred cubic alloy, CrFeCoNiPd. In the Cantor alloy, the distribution of the five constituent elements is relatively random and uniform. By contrast, in the CrFeCoNiPd alloy, in which the palladium atoms have a markedly different atomic size and electronegativity from the other elements, the homogeneity decreases considerably; all five elements tend to show greater aggregation, with a wavelength of incipient concentration waves^{11,12} as small as 1 to 3 nanometres. The resulting nanoscale alternating tensile and compressive strain fields lead to considerable resistance to dislocation glide. In situ transmission electron microscopy during straining experiments reveals massive dislocation cross-slip from the early stage of plastic deformation, resulting in strong dislocation interactions between multiple slip systems. These deformation mechanisms in the CrFeCoNiPd alloy, which differ markedly from those in the Cantor alloy and other face-centred cubic high-entropy alloys, are promoted by pronounced fluctuations in composition and an increase in stacking-fault energy, leading to higher yield strength without compromising strain hardening and tensile ductility. Mapping atomic-scale element distributions opens opportunities for understanding chemical structures and thus providing a basis for tuning composition and atomic configurations to obtain outstanding mechanical properties.

In principle, high-entropy alloys (HEAs) should form a single phase with what has been presumed to be a random solid solution¹. Some HEAs, in particular the CrCoNi-based systems, display exceptional mechanical performance, including high strength, ductility and toughness, particularly at low temperatures^{3,5}, making them potentially attractive materials for many structural applications. These special characteristics have been attributed to factors that include high entropy, sluggish diffusion and severe lattice distortion¹³, issues that are related to the degree of randomness of the solid solution. A fundamental question is whether such solid solutions with multiple principal elements involve unconventional atomic structures or elemental distributions, such as local chemical ordering or clustering, that could affect the defect behaviour and thus enhance mechanical properties. Most theoretical descriptions of solid solutions in HEAs assume that they comprise a random distribution of different atomic species. However, some simulations and more limited experimental results^{14–18}

suggest that local variations in chemical composition or even short-range order may exist in HEAs. All five elements in the most studied HEA alloy, CrMnFeCoNi, belong to the first row of transition metals in the Periodic Table, with similar atomic size and electronegativity (a measure of tendency to form intermediate compounds instead of primary solid solutions^{19,20}). How would the random alloying effect and associated solid-solution strengthening theories^{21,22} be affected if an element from another row were substituted?

To address the above questions, we investigated the atomic-scale element distributions in the CrMnFeCoNi Cantor alloy and a new CrFeCoNiPd HEA (see Methods and Extended Data Fig. 1) by using energy-dispersive X-ray spectroscopy (EDS). To obtain high-resolution EDS maps of individual elements, we used thin and clean samples, a long dwell time and low beam current to reach an appropriately high signal-to-noise ratio (see Methods). Figure 1a presents the atomic-resolution high-angle annular dark field (HAADF) images from transmission electron microscopy (TEM) and corresponding EDS maps of the CrMnFeCoNi alloy with [110] zone axis. On each EDS map for a specific element such as Cr, the brightness of an individual spot increases approximately with the number of Cr atoms in the atomic column along [110] and thus represents the local Cr density. From the EDS maps in Fig. 1a, some random density variations can be seen for all five elements, but Co, Cr and Ni share a more similar degree of homogeneity than Fe and Mn; there is little obvious evidence of assemblies of a particular element. This observation is supported by line profiles of atomic fraction taken from the EDS maps. For example, Fig. 1b shows the line profiles that represent the distribution of individual elements in a (1 $\bar{1}$ 1) plane projected along the [110] beam direction, which indicate that the atomic fraction of Co, Cr, Ni, Fe or Mn in each projected atomic column randomly fluctuates with small variation. The atomic fraction of Mn has the largest range of variation, and it occasionally reaches a high of about 30% or a low of 12%.

To identify possible repeating patterns obscured by random fluctuations, we calculated the pair correlation functions of the atomic fraction for each element (that is, autocorrelation functions) from the element line profiles represented as the sum of concentration waves^{11,12} with a spectrum of wavelengths (see Methods). Figure 1c shows the calculated pair correlation functions of individual elements for concentration wavelength r up to 3.5 nm. Generally, with such correlation function plots, a high peak at wavelength r indicates the incipient concentration wave with characteristic period r , and a wide peak reflects the gradual variation of the wave amplitude. However, Fig. 1c shows relatively low and broad peaks in the pair correlation functions for all five elements of the Cantor alloy. This indicates a lack of incipient clustering and thus confirms the observation of random element distributions with small variation from the EDS maps in Fig. 1a.

¹Center of Electron Microscopy and State Key Laboratory of Silicon Materials, Department of Materials Science and Engineering, Zhejiang University, Hangzhou, China. ²Woodruff School of Mechanical Engineering, Georgia Institute of Technology, Atlanta, GA, USA. ³Beijing Key Laboratory of Green Chemical Reaction Engineering and Technology, Department of Chemical Engineering, Tsinghua University, Beijing, China. ⁴Beijing National Laboratory for Condensed Matter Physics and Collaborative Innovation Center of Quantum Matter, Institute of Physics, Chinese Academy of Sciences, Beijing, China. ⁵Department of Materials Science and Engineering, University of Tennessee, Knoxville, TN, USA. ⁶Materials Science and Technology Division, Oak Ridge National Laboratory, Oak Ridge, TN, USA. ⁷Materials Sciences Division, Lawrence Berkeley National Laboratory, Berkeley, CA, USA. ⁸Department of Materials Science and Engineering, University of California Berkeley, Berkeley, CA, USA. ⁹These authors contributed equally: Qingqing Ding, Yin Zhang, Xiao Chen. *e-mail: ting.zhu@me.gatech.edu; roritche@lbl.gov; yu_qian@zju.edu.cn

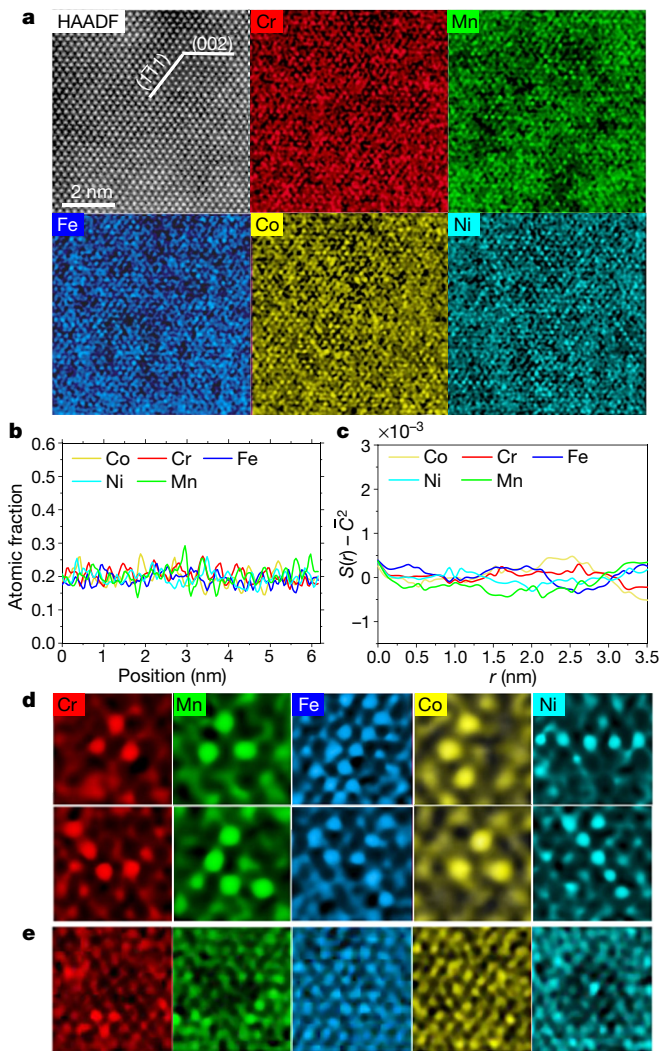


Fig. 1 | Aberration-corrected TEM imaging and mapping of element distributions in the CrMnFeCoNi Cantor alloy. **a**, HAADF image of atomic structure, taken with the $[110]$ zone axis, and corresponding EDS maps for individual elements of Cr, Mn, Fe, Co and Ni. **b**, Line profiles of atomic fraction of individual elements taken from the respective EDS maps in **a**; each line profile represents the distribution of an element in a $(1\bar{1}1)$ plane projected along the $[110]$ beam direction. **c**, Plots of pair correlation function $S(r)$ of individual elements against concentration wavelength r ; $S(r)$ is shifted by \bar{C}^2 , where \bar{C} denotes the average atomic fraction of the corresponding element. **d**, Magnification of local regions in **a** (all to same scale), showing small groups of neighbouring atomic columns with similar brightness. **e**, Comparison of the local concentration distribution of individual elements for the same region, showing that an Ni-poor region is filled by more Fe and Co than Cr and Mn.

By examining the atomic-resolution EDS maps in detail, certain local groups can be identified in the Cantor alloy, as shown in Fig. 1d. For Cr, Co and Mn, the local group can be as small as $X = 3$, where X is the number of Cr-, Co- or Mn-rich atomic columns forming a triangle or line on either the $(1\bar{1}1)$ or (002) planes. Iron tends to aggregate and displays relatively large groups. Nickel is different from the other four elements, as Ni-rich atomic columns prefer to form linear arrays on either (002) or $(1\bar{1}1)$ planes. It also appears that the Ni-poor region is filled by more Fe and Co atomic columns rather than Cr and Mn as close neighbours, as illustrated in Fig. 1e. These local groups of atomic columns may be connected to short-range ordering in random solid solutions as suggested by recent modelling studies¹⁸. However, caution should be used in interpreting these patterns, given a lack of information on the arrangement of elements along each atomic column.

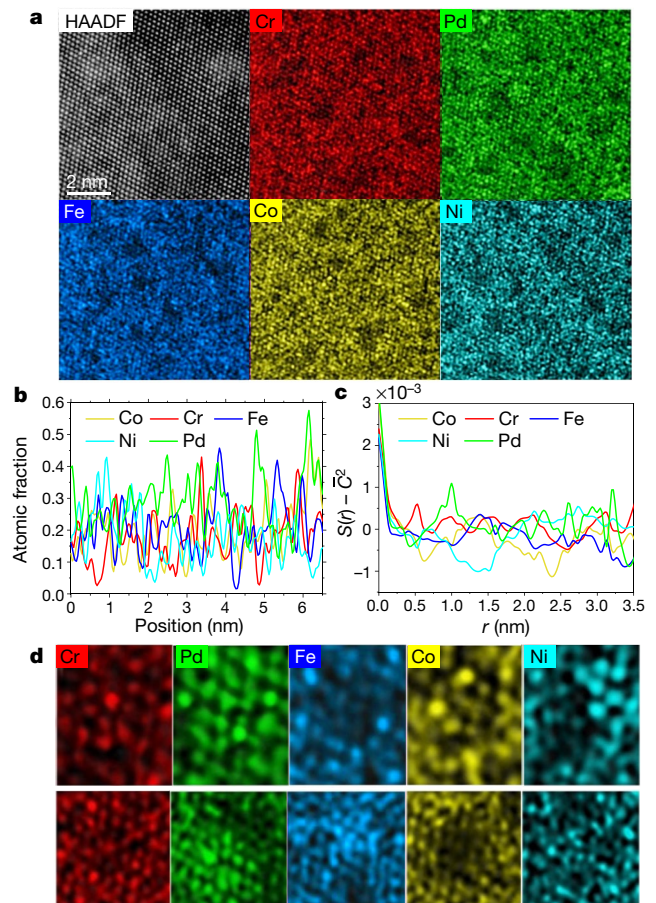


Fig. 2 | Aberration-corrected TEM imaging and mapping of element distributions in the CrFeCoNiPd alloy. **a**, HAADF image of atomic structure, taken with the $[110]$ zone axis, and corresponding EDS maps for individual elements of Cr, Fe, Co, Ni and Pd. **b**, Line profiles of atomic fraction of individual elements taken from respective EDS maps in **a**; each line profile represents the distribution of an element in a $(1\bar{1}1)$ plane projected along the $[110]$ beam direction. **c**, Plots of pair correlation functions $S(r)$ of individual elements against concentration wavelength r ; $S(r)$ is shifted by \bar{C}^2 , where \bar{C} denotes the average atomic fraction of the corresponding element. **d**, Comparison of the local concentration distribution of individual elements for the same region, showing no obvious preference for specific neighbours.

In contrast to the Cantor alloy, all five elements in the CrFeCoNiPd alloy tend to aggregate. In this HEA, the element distributions in all five EDS maps (Fig. 2a) exhibit strong inhomogeneous fluctuations with local aggregations. The corresponding line profiles (Fig. 2b) show that the atomic fraction of Fe, Co, Ni and Cr can reach 45% but decrease to 2% in regions nearby. For Pd, the fluctuation of its atomic fraction in each atomic column is even larger, with the highest atomic fraction reaching 58%. Despite strong fluctuations in element distributions in Fig. 2a, clusters with well-defined size, spacing and interface cannot be readily identified. Hence, it is more appropriate to characterize these inhomogeneous element distributions as incipient concentration waves^{11,12}. The repeating patterns of such waves are obscured by random fluctuations but can be identified by pair correlation analysis. Compared with the earlier results for the Cantor alloy (Fig. 1c), the calculated pair correlation functions for the CrFeCoNiPd alloy (Fig. 2c) reveal a strong correlation peak for Pd, Co and Fe at a concentration wavelength r around 1 nm, a similarly strong correlation peak for Ni at r around 2.5 nm, and a few weak peaks for Cr. As such, these incipient concentration waves repeat their patterns at the length scale larger than that of short-range order, which is usually considered to involve a regular arrangement of atoms within a few atomic neighbour shells, with a repeating length scale less than 0.5 nm (ref. 18). Moreover, the

correlation function peaks for Pd, Co, Fe and Ni are rather broad, indicating the diffuse interfaces of the corresponding aggregates. Overall, the results from correlation analysis indicate that these inhomogeneous element distributions have salient features of incipient concentration waves^{11,12}. In addition, the elements show no obvious preference for specific neighbours (Fig. 2d). Regions that are, for example, Ni-poor, in Fig. 2d, are not filled by a certain element but a mixture of the other four elements.

Comparison of Figs. 1 and 2 indicates that Pd atoms in the CrFeCoNiPd alloy do not simply replace Mn atoms in the CrMnFeCoNi but induce substantial changes in the distribution of all elements. In the CrFeCoNiPd alloy, Pd atoms are larger than Fe, Co, Cr and Ni. Moreover, Pd has the largest electronegativity of 6.22 (Mulliken's scale), as opposed to 4.87 for Mn and 4.77 for Cr (the latter being the smallest of the six elements in the two alloys; the electronegativity of other elements is 5.40 for Fe, 5.46 for Co and 5.85 for Ni)^{19,20}. For transition metal elements, a larger difference in electronegativity indicates a stronger tendency to form intermediate compounds instead of primary solid solutions. Hence, introducing Pd increases the individual identity of the atoms and promotes aggregations not only of Pd but also of the other four elements, resulting in pronounced chemical inhomogeneities in the alloy. In a coherent structure, an inhomogeneous element distribution inevitably gives rise to non-uniform distribution of lattice strain due to mismatch of atomic sizes. It follows that concentration waves, with characteristic wavelength as small as 1–3 nm in the CrFeCoNiPd alloy, develop through the competing action of lattice strains and concentration gradients on the system energy¹¹. Strain-induced composition modulation has been previously observed in binary and ternary alloys¹¹. However, the regularity of composition modulation is markedly reduced in the CrFeCoNiPd alloy owing to the increased complexity of local chemical bonding structures among the five constituent elements. Our atomistic Monte Carlo simulations of alloy annealing provide an example of formation of concentration waves across all the constituent elements in a model ternary alloy, which arise because of favoured bonding between certain elements as well as the lattice strain effect (see Methods and Extended Data Fig. 2).

To reveal the impact of the inhomogeneous element distribution on the microscopic deformation mechanisms, we performed in situ TEM straining experiments on the CrFeCoNiPd alloy and compared the results with those of the CrMnFeCoNi alloy. Previous studies on the CrMnFeCoNi alloy showed that in addition to $\frac{1}{2}\langle 110 \rangle \{111\}$ full dislocations, $\frac{1}{6}\langle 112 \rangle \{111\}$ partial dislocations were highly active at room temperature^{3,4}, results that were consistent with the low stacking fault energy γ_{sf} of about 30 mJ m^{-2} for the CrMnFeCoNi alloy²³. In contrast, plastic deformation in the CrFeCoNiPd alloy at room temperature primarily involved $\frac{1}{2}\langle 110 \rangle \{111\}$ full dislocations. Figure 3a presents an aberration-corrected TEM image of a 60° full dislocation consisting of two partial dislocations. From the measured dislocation core widths, the γ_{sf} was estimated to be 66 mJ m^{-2} (Extended Data Figs. 3 and 4), much higher than that of the Cantor alloy²³. In addition, dislocation motion in CrFeCoNiPd was sluggish, indicative of considerable resistance (that is, high lattice friction) to dislocation glide as indicated in Fig. 3b, which can be related to the pinning effects of pronounced concentration fluctuations in the CrFeCoNiPd alloy.

More importantly, our in situ TEM straining experiments revealed a striking phenomenon of massive cross-slip of screw dislocations in the CrFeCoNiPd alloy from the earliest stages of deformation. Such cross-slip was facilitated by the formation of a sustained dislocation pile-up, as shown in Fig. 3c and Supplementary Video 1. Because dislocations on the primary slip plane experienced high resistance to their motion, a number of dislocations in the pile-up started to cross-slip. Figure 3d shows TEM images of the massive cross-slip that was distributed almost everywhere along the dislocation pile-up. Supplementary Video 2 shows the remarkable 'rainfall'-like process of massive cross-slip. The cross-slipped dislocations frequently underwent secondary cross-slip (Supplementary Video 3), resulting in complex dislocation interactions

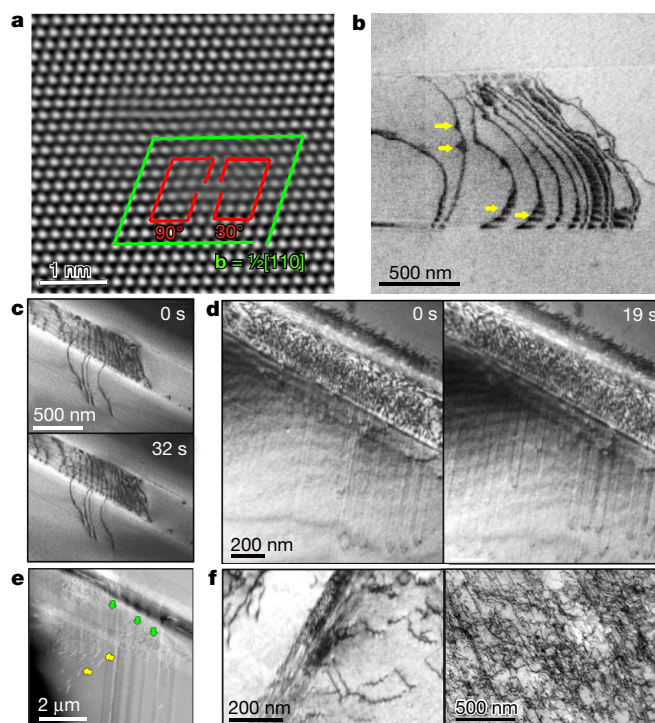


Fig. 3 | TEM observation of dislocations in the CrFeCoNiPd alloy. **a**, HAADF image taken with the $\langle 110 \rangle$ zone axis, showing the atomic structure of a 60° full dislocation, with the Burgers vector \mathbf{b} of $\frac{1}{2}[110]$. This 60° dislocation is dissociated into a 30° partial and a 90° partial. The distance between the two partials—that is, the stacking fault width—is as small as about 1 nm. **b**, TEM image taken during in situ TEM straining experiments, showing a dislocation array. Some of the moving dislocation lines exhibit widely separated leading and trailing partials (marked by yellow arrows), showing the temporary pinning of one of the partials. **c**, TEM images showing the sluggish motion of dislocations in a pile-up, where the leading dislocation was obstructed by a strong obstacle. **d**, TEM images at an early time (left image) and a late time (right image) showing massive cross-slip everywhere in the dislocation pile-up. **e**, TEM image showing the activation of new slip systems due to the interaction of intersecting slip bands. Green and yellow arrows respectively indicate the primary and secondary dislocation slip bands. **f**, Post-mortem TEM images showing dislocation microstructures in large-scale samples at the early stage of plastic deformation (left), as well as at the late stage of plastic deformation (right) with an applied large strain of about 30%, where dislocation interactions and multiplication are complex, resulting in a high dislocation density.

(Fig. 3e). Frequent cross-slip and ensuing dislocation interactions promote strain hardening, which is a reliable source of enhanced tensile ductility and toughness²⁴. To assess the thin film effect, we performed post-mortem characterization by TEM of the dislocation structures in large-scale samples at different applied strains (Fig. 3f). The results are consistent with in situ TEM observations of frequent cross-slip.

The inhomogeneous element distributions and associated deformation mechanisms can strongly influence the mechanical properties of HEAs. Figure 4a and b shows the measured uniaxial stress–strain curves, at room temperature (293 K) and at liquid nitrogen temperature (77 K), for CrFeCoNiPd and CrMnFeCoNi alloys with two different average grain sizes. At room temperature, the 0.2%-offset yield strength of the CrFeCoNiPd is 410 MPa at a grain size of about $130 \mu\text{m}$ (and 600 MPa at a grain size of about $5 \mu\text{m}$), which is higher than for the CrMnFeCoNi alloy²⁵ with a similar grain size of $155 \mu\text{m}$, and also higher than most reported HEAs with similar grain sizes^{3,6,23,25–27} (Fig. 4c and Extended Data Table 1); these strengths are also comparable to those of advanced high-strength steels^{28–30}. Furthermore, continuous steady strain hardening is achieved in CrFeCoNiPd, which is much higher than that in other single-phase HEAs with similar grain

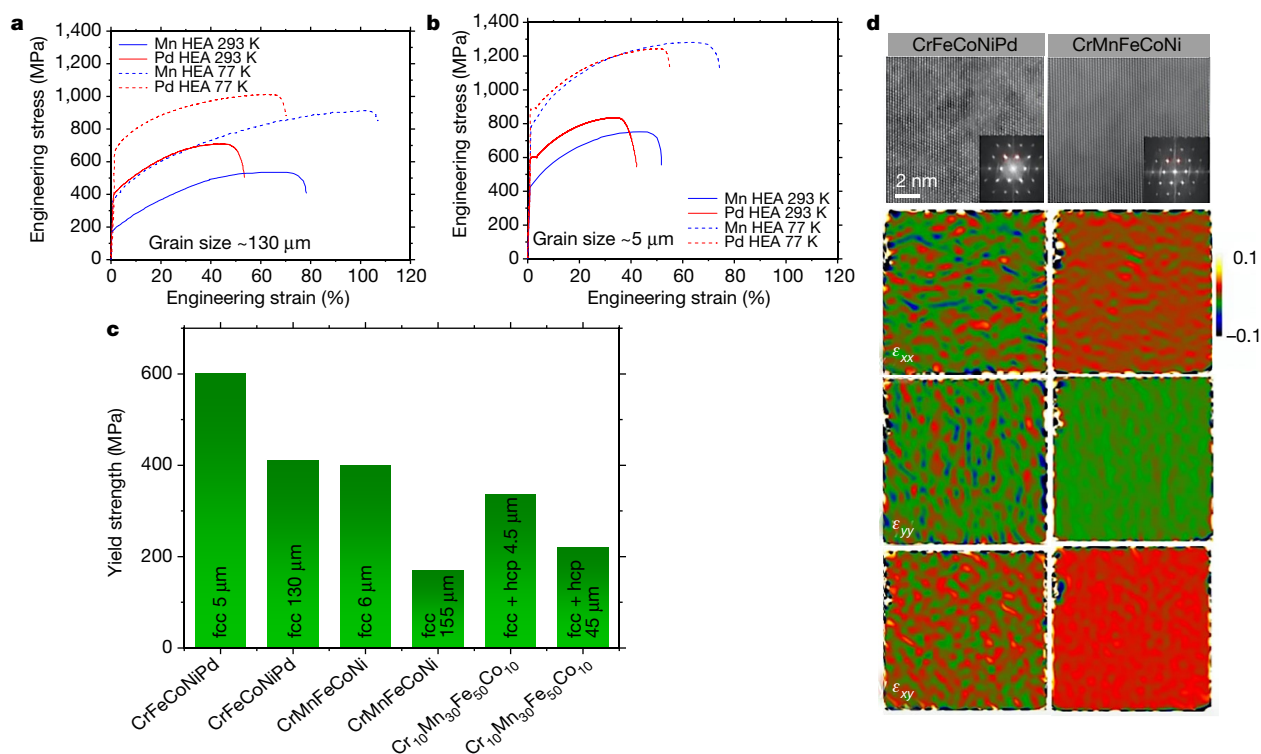


Fig. 4 | Comparison of mechanical properties of the CrFeCoNiPd alloy with other CrCoNi-based HEAs. **a**, Uniaxial tensile stress–strain curves measured at room temperature (293 K) and at liquid nitrogen temperature (77 K) for CrFeCoNiPd (marked as Pd HEA) and CrMnFeCoNi (marked as Mn HEA) with an average grain size of about 130 μm. **b**, Same as **a** except for an average grain size of about 5 μm. **c**, Comparison of yield strength between the CrFeCoNiPd alloy and other related HEAs (see the

sizes at ambient temperature^{25,31,32}. The elongation to failure is 56% at a grain size of about 130 μm (and 44% at about 5 μm grain size). The strain-hardening exponent is similar to that of other CrCoNi-based HEAs, but the hardening of CrFeCoNiPd operates at much higher stresses (Extended Data Fig. 5), leading to an exceptional combination of strength, strain hardening and ductility.

Based on the above experimental results, further insights into the composition–structure–property relationships of the CrCoNi-based HEAs are obtained through comparison of the CrFeCoNiPd and Cantor alloys. Compared with Mn, Pd plays multi-faceted roles in material hardening, including solid-solution hardening due to increased size and modulus mismatches; tuning stacking fault energy; and an increase in obstacle hardening related to aggregations of all five elements. More specifically, according to the Labusch theory^{21,22}, the degree of solid-solution hardening is largely determined by the size and modulus mismatches between the alloying and matrix atoms. From X-ray diffraction measurements, the lattice mismatch between CrFeCoNiPd (3.67 Å) and CrFeCoNi (3.57 Å) is about 3%, whereas that between CrMnFeCoNi (3.56 Å) and CrFeCoNi is less than 1%. The shear modulus mismatch between CrFeCoNiPd (approximately 89 GPa) and CrFeCoNi (approximately 82 GPa) is also about three times that between CrMnFeCoNi (approximately 80 GPa) and CrFeCoNi. Therefore, based on Labusch's theory, the CrFeCoNiPd alloy should have a stronger effect of solid-solution hardening than CrMnFeCoNi. Second, the Pd atoms in the CrFeCoNiPd alloy lead to more cross-slip by raising the average value of γ_{sf} relative to the CrMnFeCoNi alloy. In addition, introducing Pd leads to the aggregation of all five elements. The inhomogeneous element distribution modifies the local value of γ_{sf} in the dislocation core, an effect that could lower the effective energy barrier for cross-slip³³. Third, the inhomogeneous element distribution also modifies the distribution of lattice friction, resulting in stronger resistance to dislocation motion

yield strength data in Extended Data Table 1), which have the pure fcc phase or combined fcc and hexagonal close-packed (hcp) phases. **d**, Comparison of atomic strain distribution between the CrFeCoNiPd and CrMnFeCoNi alloys, based on HAADF image and corresponding maps of horizontal normal strain (ϵ_{xx}), vertical normal strain (ϵ_{yy}) and shear strain (ϵ_{xy}).

than in the Cantor alloy. As shown by the strain maps (see Methods) in Fig. 4d, the atomic strain fields in the CrMnFeCoNi alloy are more uniform, whereas substantial atomic strain fluctuations exist in the CrFeCoNiPd alloy. Although the distribution of atomic strain fields appears random at the nanoscale, the tensile and compressive strain fields alternate, which presumably leads to large local internal stresses and thus resistance to dislocation glide.

To further demonstrate the tunability of element distributions in HEAs, we used the element Al to replace Mn and obtained a face-centred cubic (fcc) Cr₂₀Fe₂₀Co₁₈Ni₃₀Al₁₂ alloy. Pronounced composition fluctuations in the form of concentration waves and frequent cross-slip were again observed (Extended Data Fig. 6). As a further example of the formation of concentration waves by tuning the alloy composition, we added 5 at% W into a medium-entropy alloy of CrCoNi. The results (Extended Data Fig. 7) show that W atoms can effectively reduce the homogeneity of chemical distribution and enhance the strengthening effect.

The atomic-scale mapping of chemical distribution and associated correlation analysis (including autocorrelation and cross-correlation) open opportunities for resolving the nanoscale chemical structures not only in HEAs but also in other solid solutions more generally. The insight gained into the relationships between chemical structure, microstructure and properties may provide a fundamental basis for tuning compositions and atomic configurations to produce new deformation mechanisms and mechanical properties in HEAs.

Online content

Any methods, additional references, Nature Research reporting summaries, source data, extended data, supplementary information, acknowledgements, peer review information; details of author contributions and competing interests; and statements of data and code availability are available at <https://doi.org/10.1038/s41586-019-1617-1>.

Received: 4 April 2017; Accepted: 31 July 2019;
Published online 9 October 2019.

1. Yeh, J. W. et al. Nanostructured high-entropy alloys with multiple principal elements: Novel alloy design concepts and outcomes. *Adv. Eng. Mater.* **6**, 299–303 (2004).
2. Cantor, B., Chang, I. T. H., Knight, P. & Vincent, A. J. B. Microstructural development in equiatomic multicomponent alloys. *Mater. Sci. Eng. A* **375–377**, 213–218 (2004).
3. Gludovatz, B. et al. A fracture-resistant high-entropy alloy for cryogenic applications. *Science* **345**, 1153–1158 (2014).
4. Zhang, Z. J. et al. Nanoscale origins of the damage tolerance of the high-entropy alloy CrMnFeCoNi. *Nat. Commun.* **6**, 10143 (2015).
5. Gludovatz, B. et al. Exceptional damage-tolerance of a medium-entropy alloy CrCoNi at cryogenic temperatures. *Nat. Commun.* **7**, 10602 (2016).
6. Li, Z. M., Pradeep, K. G., Deng, Y., Raabe, D. & Tسان, C. C. Metastable high-entropy dual-phase alloys overcome the strength-ductility trade-off. *Nature* **534**, 227–230 (2016).
7. Lei, Z. et al. Enhanced strength and ductility in a high-entropy alloy via ordered oxygen complexes. *Nature* **563**, 546–550 (2018).
8. Yang, T. et al. Multicomponent intermetallic nanoparticles and superb mechanical behaviors of complex alloys. *Science* **362**, 933–937 (2018).
9. Zhang, Y. et al. Microstructures and properties of high-entropy alloys. *Prog. Mater. Sci.* **61**, 1–93 (2014).
10. Miracle, D. B. & Senkov, O. N. A critical review of high entropy alloys and related concepts. *Acta Mater.* **122**, 448–511 (2017).
11. Khachaturian, A. G. *Theory of Structural Transformations in Solids* (Dover, 2013).
12. Gyorffy, B. L. & Stocks, G. M. Concentration waves and Fermi surfaces in random metallic alloys. *Phys. Rev. Lett.* **50**, 374–377 (1983).
13. Gludovatz, B., George, E. P. & Ritchie, R. O. Processing, microstructure and mechanical properties of the CrMnFeCoNi high-entropy alloy. *JOM* **67**, 2262–2270 (2015).
14. Widom, M., Huhn, W. P., Maiti, S. & Steurer, W. Hybrid Monte Carlo/molecular dynamics simulation of a refractory metal high entropy alloy. *Mater. Mater. Trans. A* **45**, 196–200 (2014).
15. Tamm, A., Aabloo, A., Klintenberg, M., Stocks, M. & Caro, A. Atomic-scale properties of Ni-based FCC ternary, and quaternary alloys. *Acta Mater.* **99**, 307–312 (2015).
16. Zhang, F. X. et al. Local structure and short-range order in a NiCoCr solid solution alloy. *Phys. Rev. Lett.* **118**, 205501 (2017).
17. Ma, Y. et al. Chemical short-range orders and the induced structural transition in high-entropy alloys. *Scr. Mater.* **144**, 64–68 (2018).
18. Ding, J., Yu, Q., Asta, M. & Ritchie, R. O. Tunable stacking fault energies by tailoring local chemical order in CrCoNi medium-entropy alloys. *Proc. Natl Acad. Sci. USA* **115**, 8919–8924 (2018).
19. Watson, R. E. & Bennett, L. H. Transition metals: *d*-band hybridization, electronegativities and structural stability of intermetallic compounds. *Phys. Rev. B* **18**, 6439–6449 (1978).
20. Cottrell, A. H. *Concepts of the Electron Theory of Alloys* (IOM Communications, 1998).
21. Labusch, R. A statistical theory of solid solution hardening. *Phys. Status Solidi* **41**, 659–669 (1970).
22. Nabarro, F. R. N. Theory of solution hardening. *Philos. Mag.* **35**, 613–622 (1977).
23. Okamoto, N. L. et al. Size effect, critical resolved shear stress, stacking fault energy, and solid solution strengthening in the CrMnFeCoNi high-entropy alloy. *Sci. Rep.* **6**, 35863 (2016).
24. Hart, E. W. Theory of tensile test. *Acta Metall.* **15**, 351–355 (1967).
25. Otto, F. et al. The influences of temperature and microstructure on the tensile properties of a CoCrFeMnNi high-entropy alloy. *Acta Mater.* **61**, 5743–5755 (2013).
26. Wu, Z., Bei, H., Pharr, G. M. & George, E. P. Temperature dependence of the mechanical properties of equiatomic solid solution alloys with face-centered cubic crystal structures. *Acta Mater.* **81**, 428–441 (2014).
27. Liu, W. H. et al. Ductile CoCrFeNiMo_x high entropy alloys strengthened by hard intermetallic phases. *Acta Mater.* **116**, 332–342 (2016).
28. Kim, S.-H., Kim, H. & Kim, N. J. Brittle intermetallic compound makes ultrastrong low-density steel with large ductility. *Nature* **518**, 77–79 (2015).
29. Jacques, P. J., Furnémont, Q., Lani, F., Pardoën, T. & Delannay, F. Multiscale mechanics of TRIP-assisted multiphase steels. I. Characterization and mechanical testing. *Acta Mater.* **55**, 3681–3693 (2007).
30. Bouaziz, O., Allain, S., Scott, C. P., Cugy, P. & Barbier, D. High manganese austenitic twinning induced plasticity steels: a review of the microstructure properties relationships. *Curr. Opin. Solid State Mater. Sci.* **15**, 141–168 (2011).
31. Ma, S. G. et al. Superior high tensile elongation of a single-crystal CoCrFeNiAl_{0.3} high-entropy alloy by Bridgman solidification. *Intermetallics* **54**, 104–109 (2014).
32. Zaddach, A. J., Scattergood, R. O. & Koch, C. C. Tensile properties of low-stacking fault energy high-entropy alloys. *Mater. Sci. Eng. A* **636**, 373–378 (2015).
33. Nöhning, W. G. & Curtin, W. A. Cross-slip of long dislocations in FCC solid solutions. *Acta Mater.* **158**, 95–117 (2018).

Publisher's note Springer Nature remains neutral with regard to jurisdictional claims in published maps and institutional affiliations.

© The Author(s), under exclusive licence to Springer Nature Limited 2019

METHODS

Experimental. The CrMnFeCoNi alloy was processed as previously reported²⁵. Using the same method, the CrFeCoNiPd alloy was produced by arc-melting pure Fe, Co, Ni, Cr and Pd metals (>99.9% purity). To ensure thorough mixing of all elements, the arc-melted buttons were flipped and re-melted at least five times, followed by drop-casting into Cu moulds to produce rectangular ingots with the dimensions $12.7 \times 12.7 \times 70 \text{ mm}^3$. The rectangular bars were homogenized in vacuo at $1,200^\circ\text{C}$ for 24 h before rolling into 1.8-mm-thick plates at room temperature. Single fcc phase was obtained and confirmed by X-ray diffraction (Extended Data Fig. 1). Equiaxed grain microstructures with average grain sizes of about $130 \mu\text{m}$ and $5 \mu\text{m}$ were obtained by recrystallizing at $1,150^\circ\text{C}$ for 1 h and 20 min in vacuum, respectively.

Atomic-resolution EDS mapping was performed with an aberration-corrected scanning transmission electron microscope (STEM, FEI Titan Cubed Themis G2 300) operated at 300 kV with a convergence semi-angle of 23.6 mrad . The microscope was equipped with a DCOR plus spherical aberration corrector for the electron probe which was aligned before every experiment by using a gold standard sample. The experiments were performed with the following aberration coefficients: A1 = 1.41 nm; A2 = 11.5 nm; B2 = 22.2 nm; C3 = 2.05 μm ; A3 = 525 nm; S3 = 177 nm; A4 = 8.81 μm , D4 = 2.39 μm , B4 = 13.2 μm , C5 = -3.95 nm, A5 = 295 μm , S5 = 111 μm , and R5 = 102 μm , ensuring 0.06 nm resolution under normal conditions. The beam current was set between 25 pA and 30 pA. The dwell time was 1 μs per pixel with a map size of 256×256 pixels; a complete process of EDS mapping took roughly 1.5 h to reach an appropriately high signal-to-noise ratio. The samples were thinned down by jet polish and Ar ion cleaning. Pre-cracked 3 mm TEM grids were pulled to fracture for making ultra-thin areas.

For in situ TEM straining tests, samples were prepared using a twin-jet electropolisher in an acetic acid solution containing 10 vol% perchloric acid at 30 mA and 10°C . The electron-transparent area was placed on the rectangular hole of the tension substrate and the sample was glued to the tension substrate. We then mounted the tensile sample onto a Gatan single-tilt straining holder with two screws. In situ straining experiments were conducted in an FEI Tecnai G2 F20 TEM operating at 200 kV. The in situ straining tests were conducted in a displacement-control mode.

For bulk mechanical tests, flat tensile specimens with a dog-bone shape and a gauge length of 10 mm were cut from the recrystallized sheets by electrical discharge machining. The tensile axis was perpendicular to the rolling direction. The gauge sections were carefully ground down to 600-grit SiC paper. Uniaxial tensile tests were performed with a screw-driven tensile testing machine (Instron) at a strain rate of 10^{-3} s^{-1} and temperatures of 77 K or 293 K. For the 77 K tests, the specimens and grips were entirely immersed in a bath of liquid nitrogen. Room-temperature tests were performed in a laboratory room environment.

Atomic strain maps were obtained using the geometric phase analysis method³⁴. We took over 50 aberration-corrected TEM images of the same region and averaged the corresponding atomic positions, so as to minimize the possible influence of vibration during scanning on the strain maps. Although such atomic strain analysis is affected by camera resolution, the qualitative difference in atomic strain maps between the two alloys studied is substantial, indicating the qualitative difference in lattice distortion between the two alloys.

Correlation analysis. To find the repeating patterns of element distribution, we calculated pair correlation functions from line profiles of atomic fraction taken from the EDS maps. For each correlation function calculation, seven line profiles for an individual element were used to obtain the ensemble average. For example, the line profile of the atomic fraction of Cr, $C_{\text{Cr}}(x)$, is measured as a function of spatial coordinate x along the [112] direction. The corresponding pair correlation function is defined as $S_{\text{Cr}-\text{Cr}}(r) = \langle C_{\text{Cr}}(x) \cdot C_{\text{Cr}}(x+r) \rangle$, where $C_{\text{Cr}}(x) \cdot C_{\text{Cr}}(x+r)$ is the product between the atomic fractions of Cr at two points with separation r , and the symbol $\langle \rangle$ denotes the ensemble average of $C_{\text{Cr}}(x) \cdot C_{\text{Cr}}(x+r)$ over all possible positions x for a fixed r . According to the Wiener-Khinchine theorem³⁵, the pair correlation function for each element (that is, autocorrelation function) can be related to the power spectral density of the line profile of atomic fraction via the Fourier transform. As such, when the line profiles are considered to consist of a series of concentration waves^{12,13} with a spectrum of wavelengths, the high peak at wavelength r on the correlation function plot indicates the incipient concentration wave with the characteristic period r . Hence, pair correlation functions can be used to identify the primary repeating patterns on line profiles obscured by random fluctuations.

To calculate the pair correlation function using the discrete data points of a line profile, the above-defined correlation function can be expressed as $S_{\text{Cr}-\text{Cr}}(r) = \frac{1}{N} \sum_{r < (y-x) < r + \Delta r} C_{\text{Cr}}(x) \cdot C_{\text{Cr}}(y)$ where N is the total number of pairs of $C_{\text{Cr}}(x)$ and $C_{\text{Cr}}(y)$; here $C_{\text{Cr}}(y)$ denotes the atomic fraction of Cr at the coordinate

y that falls in the range $r < (y-x) < r + \Delta r$, that is, when y is close to $x + r$ but can vary within a small range of Δr . In our calculations, Δr was taken as 0.66 \AA . In this way, the correlation function peak associated with the periodic lattice (that is, with the period of the lattice constant) can be filtered out on the pair correlation function plot, revealing the repeating patterns whose period is larger than the lattice constant (that is, beyond the nearest neighbour distance). Owing to concentration fluctuations, there is a certain variability of the average value of atomic fraction for each element. To aid comparison between pair correlation functions of different elements, the plot of $S_{\text{Cr}-\text{Cr}}(r)$ for each element is shifted by the square of the average atomic fraction, \bar{C}_{Cr}^2 . The final plot of $S_{\text{Cr}-\text{Cr}}(r) - \bar{C}_{\text{Cr}}^2$ can be used to identify the periodic patterns obscured by random fluctuations.

Monte Carlo simulation. We conducted atomistic Monte Carlo simulations of alloy annealing to gain insights into the mechanisms underlying the concentration waves revealed by atomic-resolution EDS mapping. That is, we first set up the fcc structure of a model equiatomic alloy with a random element distribution. The cubic supercell had a side length of 10.7 nm and contained a total of 108,000 atoms. Periodic boundary conditions were applied to the supercell. At a given annealing temperature, this structure was relaxed to lower the system energy by element rearrangement through the Monte Carlo algorithm implemented by the molecular dynamics code LAMMPS³⁶. During this simulated annealing process, concentration waves developed across all elements, mainly owing to different bonding energies/preferences between elements. These concentration waves, with a characteristic wavelength of about 2 nm, correspond to a mixture of two coexisting phases with different compositions. The simulated EDS maps and pair correlation function plots strongly resemble our experimental results. Further, Monte Carlo simulations show that the wavelengths of simulated concentration waves vary with annealing temperature, indicating the tunability of chemical structures by annealing temperature.

More specifically, as shown in Extended Data Fig. 2a, we set up an initial random alloy structure for a model ternary alloy, referred to as the ABC alloy. The interatomic potential of this alloy was developed to model the CrCoNi alloy³⁷ and gives different bonding energies and preferences among the three constituent elements. As a result, this model alloy system favours the formation of two coexisting fcc phases with different compositions: that is, one fcc phase predominantly consists of a mixture of elements A and B, and the other fcc phase is primarily composed of element C. Such two-phase chemical structures arise mainly from the favoured chemical bonding between elements A and B. Starting from a random alloy structure in Extended Data Fig. 2a, the Monte Carlo simulation at an annealing temperature of 800 K resulted in the relaxed atomic structure in Extended Data Fig. 2b. Clearly, a mixture of two coexisting phases has developed, with a complex morphology of aggregates of each phase. Extended Data Fig. 2c shows the simulated EDS map for element C based on the relaxed structure in Extended Data Fig. 2b, for a sample thickness of 8 nm along the [110] zone axis, similar to the TEM sample. It is seen that the concentration of element C varies with a characteristic wavelength of about 2 nm. The other two elements also exhibit similar concentration wave patterns in simulated EDS maps. The characteristic wavelengths around about 2 nm for all the elements are confirmed by their pair correlation function peaks in Extended Data Fig. 2d.

To summarize, our Monte Carlo simulations demonstrate the formation of concentration waves across all the constituent elements in a model alloy. This primarily arises from the favoured bonding between certain transition metal elements that is caused by their large difference in electronegativity. The different atomic sizes help to maintain the stability of these concentration waves after more than 10^6 Monte Carlo steps of structural relaxation, owing to the competing effects of lattice strains and concentration gradients on the system energy.

Reporting summary. Further information on research design is available in the Nature Research Reporting Summary linked to this paper.

Data availability

All data generated or analysed during this study are included in the published article and Supplementary Information, and are available from the corresponding authors upon reasonable request.

- Hytch, M. J., Snoeck, E. & Kilaas, R. Quantitative measurement of displacement and strain fields from HREM micrographs. *Ultramicroscopy* **74**, 131–146 (1998).
- Chatfield, C. *The Analysis of Time Series: An Introduction* 6th edn (Chapman and Hall/CRC, 2003).
- Plimpton, S. Fast parallel algorithms for short-range molecular dynamics. *J. Comput. Phys.* **117**, 1–19 (1995).
- Li, Q., Sheng, H. & Ma, E. Strengthening in multi-principal element alloys with local-chemical-order roughened dislocation pathways. *Nat. Commun.* **10**, 3563 (2019).

Acknowledgements Q.Y. was supported by the National Natural Science Foundation of China (51671168), National Key Research and Development

Program of China (2017YFA0208200), 111 project under grant no. B16042, and the State Key Program for Basic Research in China under grant no. 2015CB659300. T.Z. was supported by the US National Science Foundation under grant no. DMR-1810720. R.O.R. was supported by the US Department of Energy, Office of Science, Office of Basic Energy Sciences, Materials Sciences and Engineering Division and under contract no. DE-AC02-05CH11231 to the Mechanical Behavior of Materials program (KC13) at the Lawrence Berkeley National Laboratory. We thank E. Ma for providing the interatomic potential used for Monte Carlo simulations.

Author contributions Q.Y., T.Z. and R.O.R. designed the research. Q.Y., Q.D., X.F., X.C., S.C., L.G. and F.W. performed TEM and in situ experiments. H.B. synthesized alloys and conducted mechanical testing. Y.Z., D.C., Y.G., M.W., T.Z. and Q.Y. conducted data analysis and modelling. Q.Y., T.Z., R.O.R., Q.D., Z.Z., J.L.

and H.B. wrote the manuscript. All authors contributed to the discussion and revision of the paper.

Competing interests The authors declare no competing interests.

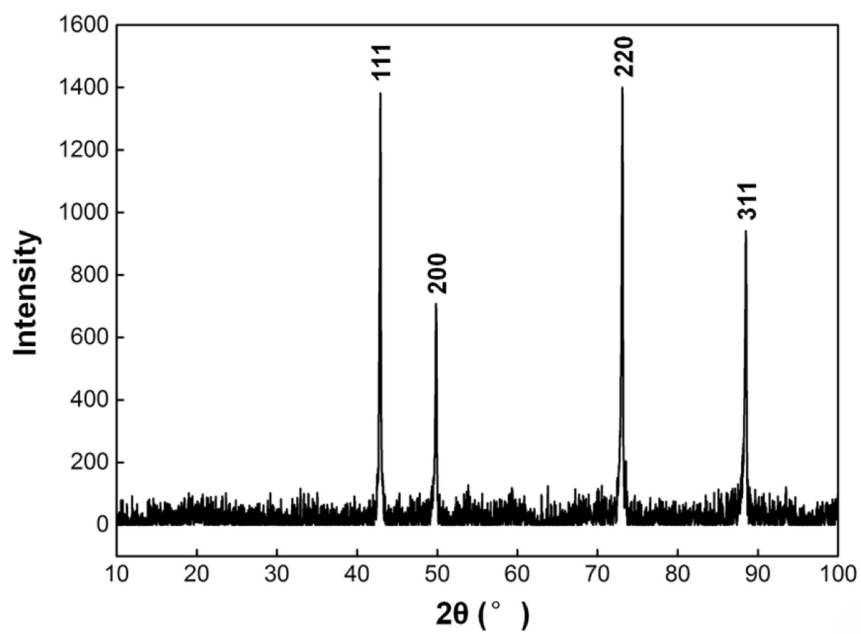
Additional information

Supplementary information is available for this paper at <https://doi.org/10.1038/s41586-019-1617-1>.

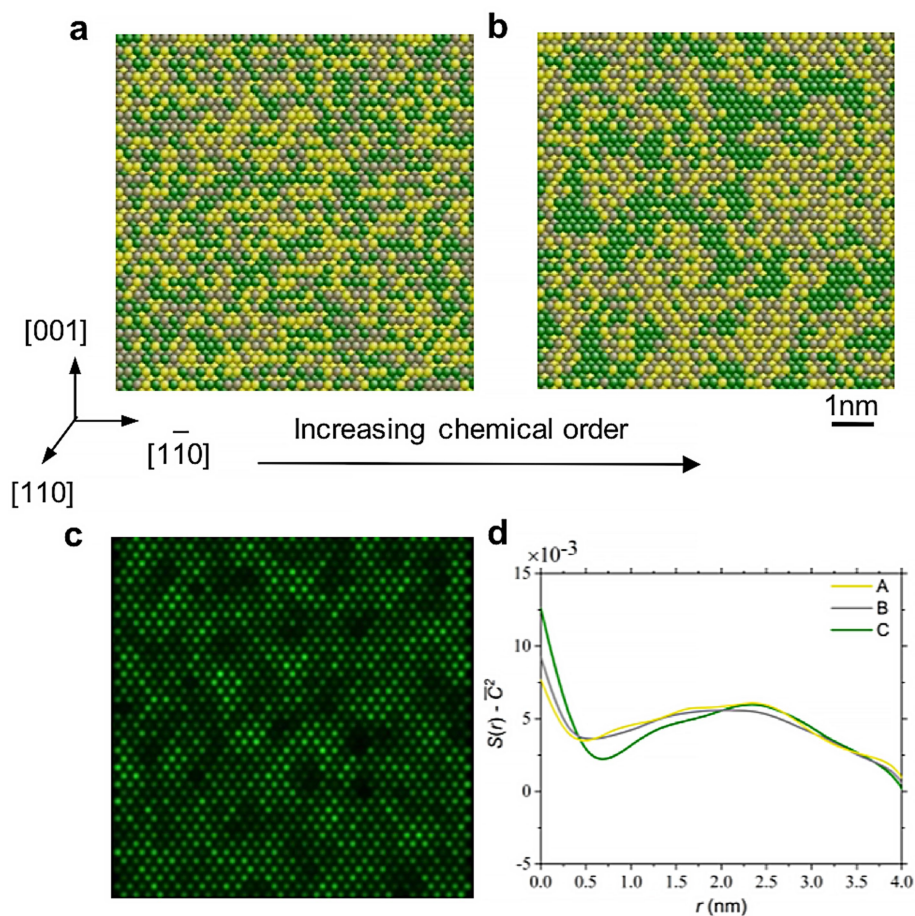
Correspondence and requests for materials should be addressed to T.Z., R.O.R. or Q.Y.

Peer review information *Nature* thanks Elena Pereloma and the other, anonymous, reviewer(s) for their contribution to the peer review of this work.

Reprints and permissions information is available at <http://www.nature.com/reprints>.

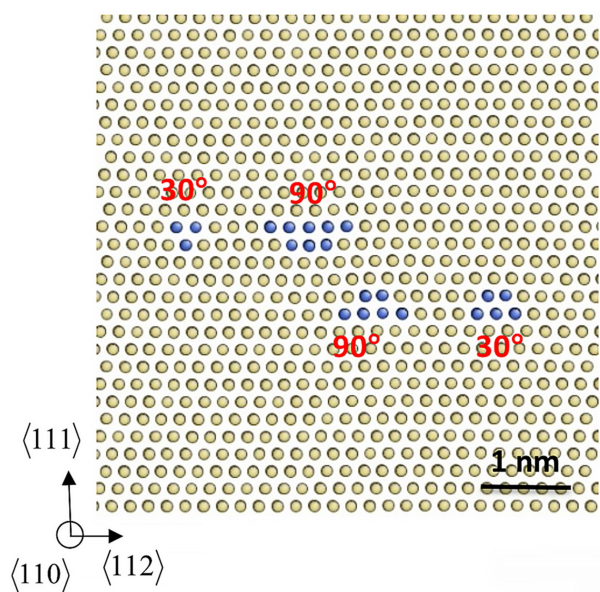


Extended Data Fig. 1 | X-ray diffraction characterization showing the single-phase signal of the fcc structure of the CrFeCoNiPd alloy.

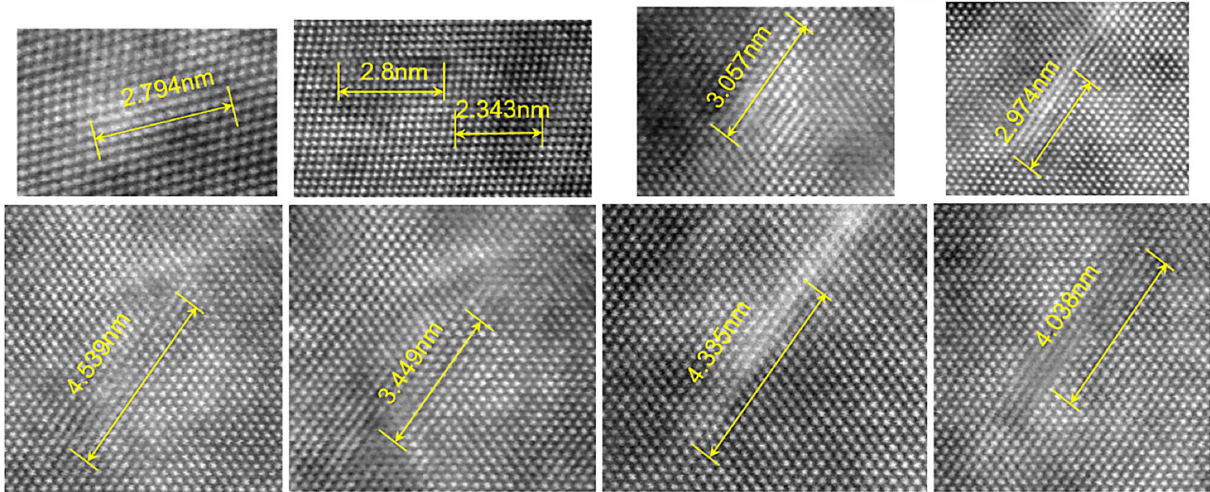


Extended Data Fig. 2 | Atomistic Monte Carlo simulation. Simulation shows formation of concentration waves in a model equiatomic ternary alloy under annealing at a temperature of 800 K. **a**, Initial fcc structure with a random distribution of the three constituent elements; yellow, grey and green atoms represent A, B and C elements, respectively. **b**, Relaxed

structure showing the formation of a mixture of an element-A/B dominant phase (mixed yellow and grey atoms) and an element-C dominant phase (green atom clusters). **c**, Simulated EDS map for element C based on the structure in **b**. **d**, Plots of pair correlation functions $S(r)$ of individual elements against concentration wavelength r .

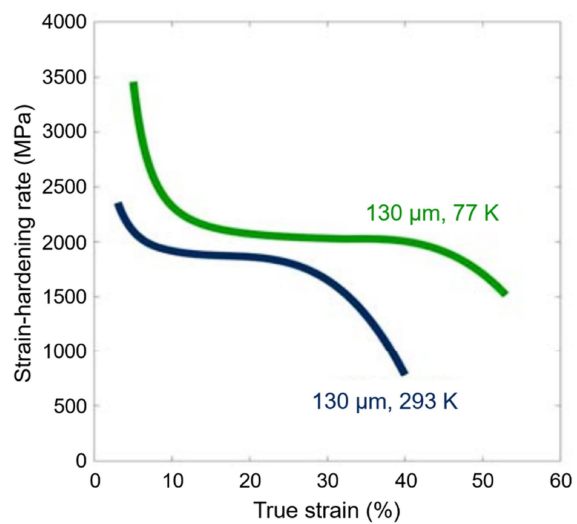


Extended Data Fig. 3 | Atomic structure of a simulated dislocation dipole. The structure consists of two closely spaced 60° dislocations of opposite signs in an fcc Ni single crystal, for comparison with similar dislocation core structures in Fig. 3a. Atoms are coloured by their coordination numbers (CN = 12, yellow; CN = 11, blue), so as to display 30° and 90° partial dislocations (atoms in blue) in the core of an extended 60° full dislocation.

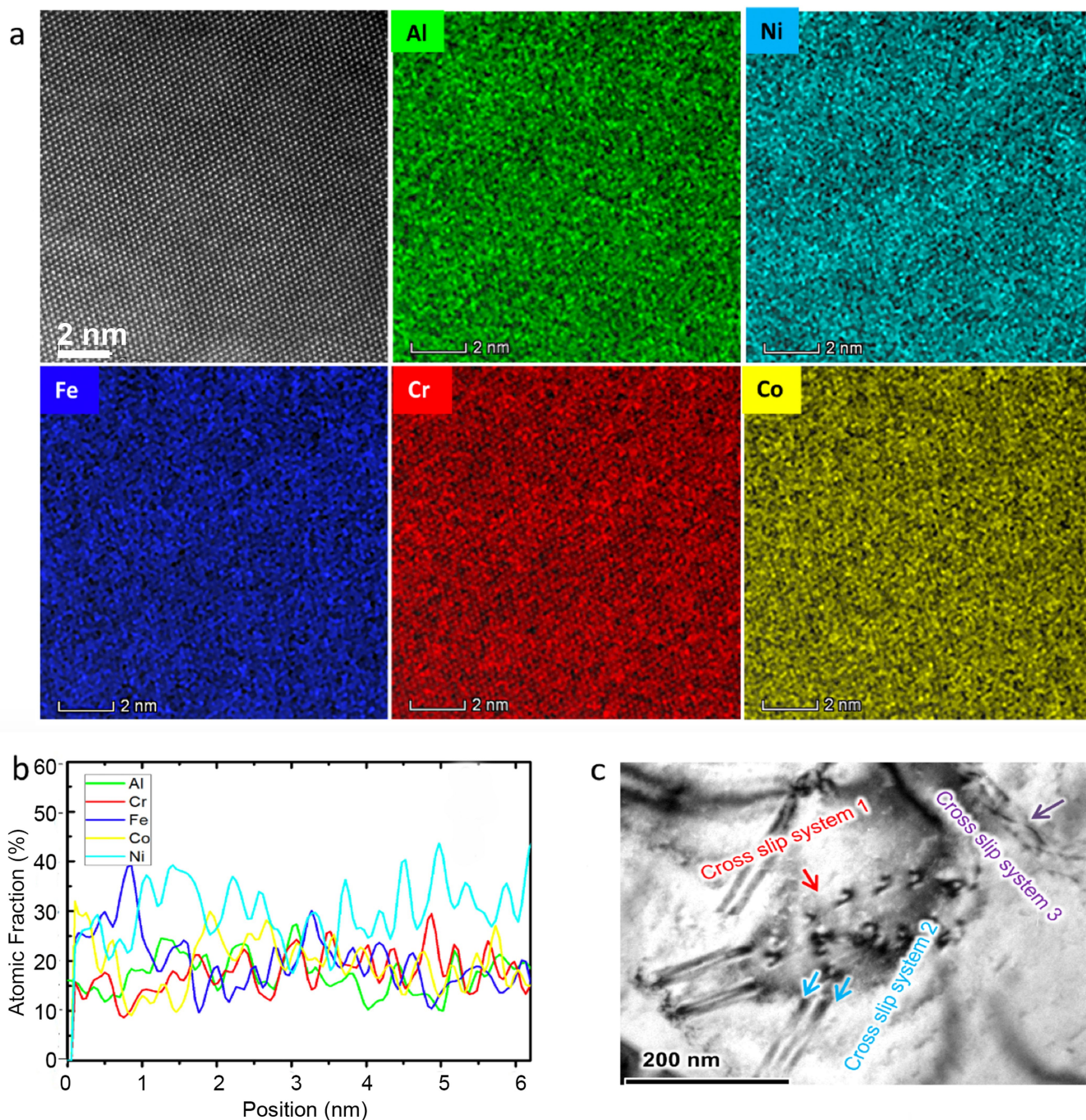


Extended Data Fig. 4 | High-resolution TEM images of the cores of dissociated 60° dislocations in the CrFeCoNiPd alloy. The number in each image indicates the measured stacking fault width in the core of dissociated dislocation. The average stacking fault width is $d = 3.37$ nm. The stacking-fault energy γ_{sf} can be estimated as

$\gamma_{sf} = \frac{\mu b_p^2}{8\pi d} \left(\frac{2-\nu}{1-\nu} \right) \left(1 - \frac{2\nu \cos 2\theta}{2-\nu} \right)$, where θ is the angle between the dislocation line and the Burgers vector of the full dislocation, b_p is the length of the Burgers vector of the partial dislocation, μ is the shear modulus and ν is Poisson's ratio. The γ_{sf} of the CrFeCoNiPd alloy is estimated to be 66 mJ m^{-2} .

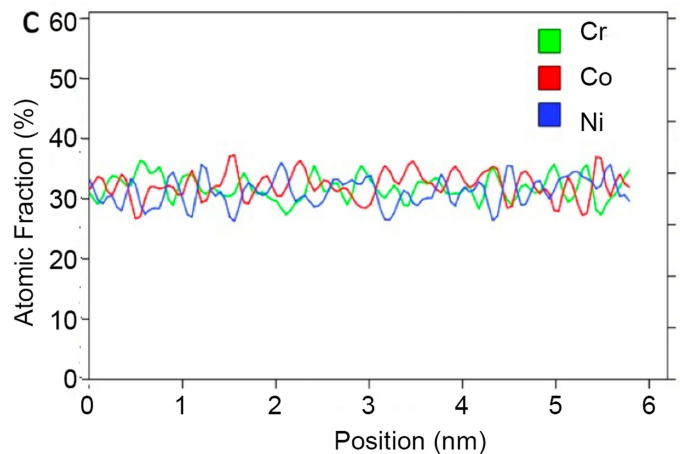
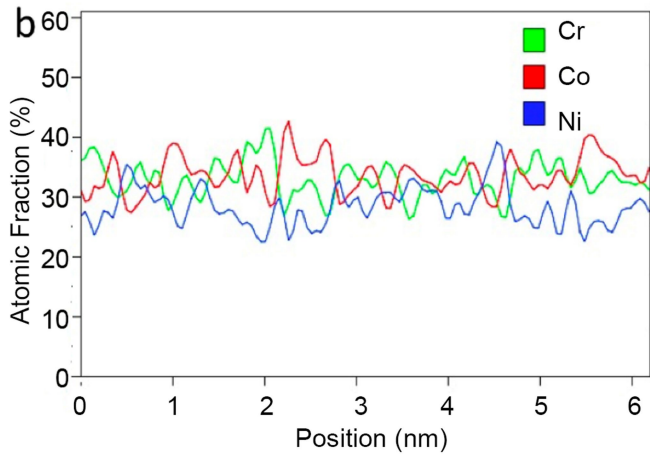
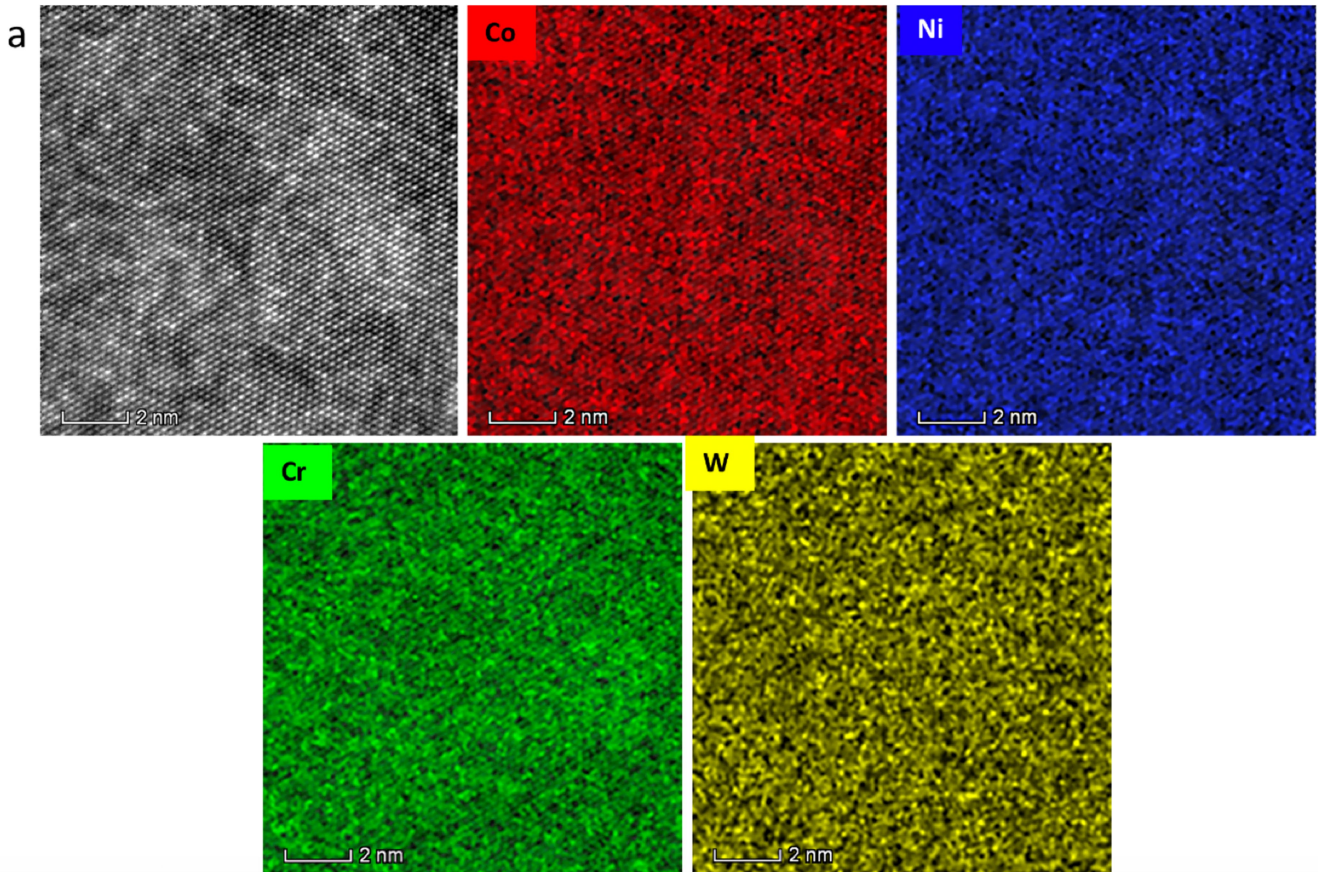


Extended Data Fig. 5 | Kocks–Mecking plots. The plots of strain hardening rate against true strain at 293 K and 77 K show the strong hardening capability of the CrFeCoNiPd alloy.



Extended Data Fig. 6 | Aberration-corrected TEM imaging and mapping of element distributions in the $\text{Cr}_{20}\text{Fe}_{20}\text{Co}_{18}\text{Ni}_{30}\text{Al}_{12}$ alloy. **a**, HAADF images and associated EDS maps (taken along the $[110]$ zone axis) for individual elements of Cr, Fe, Co, Ni and Al. **b**, Line profiles of atomic fraction of individual elements taken from respective EDS

maps in **a**; each line profile represents the distribution of an element in a (002) plane projected along the $[110]$ beam direction. **c**, Cross-slip of dislocations in the $\text{Cr}_{20}\text{Fe}_{20}\text{Co}_{18}\text{Ni}_{30}\text{Al}_{12}$ alloy, from in situ straining experiment.



Extended Data Fig. 7 | Comparison of element distributions in CrCoNi alloy and in CrCoNi alloy containing 5 at% W. a, HAADF image and corresponding EDS maps of the CrCoNi alloy containing 5 at% W, taken along the $[110]$ zone axis, showing the distribution of individual elements of Cr, Co, Ni and W. b, Line profiles of atomic fraction of elements Cr, Co and Ni taken from respective EDS maps in a for the CrCoNi alloy

containing 5 at% W; each line profile represents the distribution of an element in a $(\bar{1}\bar{1}1)$ plane projected along the $[110]$ beam direction. c, Line profiles of atomic fraction of individual elements taken from the corresponding EDS maps of the CrCoNi alloy; each line profile represents the distribution of an element in a $(\bar{1}\bar{1}1)$ plane projected along the $[110]$ beam direction.

Extended Data Table 1 | Properties of the CrMnFeCoNi, CrFeCoNiPd, Cr₁₀Mn₃₀Fe₅₀Co₁₀ and CrCoNi alloys

| Alloy | Grain size (μm) | Temperature (K) | σ_y (MPa) | σ_{UTS} (MPa) | ε_f (%) | n |
|----------------------------------------------------------------------------------|---------------------------------|--------------------|---------------------|--------------------------------|------------------------|------|
| CrMnFeCoNi ³ | 6 | 293 | 410 | 763 | 57 | 0.41 |
| CrMnFeCoNi ³ | 6 | 77 | 759 | 1280 | 71 | 0.36 |
| CrFeCoNiPd | 135 | 293 | 410 | 710 | 56 | 0.33 |
| CrFeCoNiPd | 135 | 77 | 666 | 1012 | 74 | 0.39 |
| CrFeCoNiPd | 5 | 293 | 604 | 835 | 44 | 0.38 |
| CrFeCoNiPd | 5 | 77 | 900 | 1244 | 60 | 0.38 |
| Cr ₁₀ Mn ₃₀ Fe ₅₀ Co ₁₀ ⁶ | 4.5 | 293 | 337 | 872 | 74 | n/a |
| Cr ₁₀ Mn ₃₀ Fe ₅₀ Co ₁₀ ⁶ | 45 | 293 | 220 | 730 | 51 | n/a |
| CrCoNi ⁵ | 5-50 | 293 | 440 | 884 | 73 | 0.40 |
| CrCoNi ⁵ | 5-50 | 77 | 657 | 1311 | 90 | 0.40 |

Yield strength (σ_y), ultimate tensile strength (σ_{UTS}), elongation to failure strain (ε_f) and strain-hardening exponent (n) of the CrMnFeCoNi, CrFeCoNiPd, Cr₁₀Mn₃₀Fe₅₀Co₁₀ and CrCoNi alloys at room and cryogenic temperatures.